PNAS RESEARCH ARTICLE | MICROBIOLOGY

Bispecific antibodies targeting two glycoproteins on SFTSV exhibit synergistic neutralization and protection in a mouse model

Zhen Chang[a,1], Dan Gao[a,1], Liying Liao[a,1], Junqing Sun[b,c,1], Gen Zhang[b,d], Xue Zhang[a], Feiran Wang[b], Chunrui Li[b], Babayemi Olawale Oladejo[b,e], Shihua Li[b], Yan Chai[b], Yongfei Hu[f], Xuancheng Lu[g], Haixia Xiao[h], Jianxun Qi[b], Zhihai Chen[i,2], Feng Gao[h,2], and Yan Wu[a,2]

Edited by Rafi Ahmed, Emory University, Atlanta, GA; received January 8, 2024; accepted April 8, 2024

Severe fever with thrombocytopenia syndrome (SFTS) is an emerging infectious disease with a high fatality rate of up to 30% caused by SFTS virus (SFTSV). However, no specific vaccine or antiviral therapy has been approved for clinical use. To develop an effective treatment, we isolated a panel of human monoclonal antibodies (mAbs). SF5 and SF83 are two neutralizing mAbs that recognize two viral glycoproteins (Gn and Gc), respectively. We found that their epitopes are closely located, and we then engineered them as several bispecific antibodies (bsAbs). Neutralization and animal experiments indicated that bsAbs display more potent protective effects than the parental mAbs, and the cryoelectron microscopy structure of a bsAb3 Fab–Gn–Gc complex elucidated the mechanism of protection. In vivo virus passage in the presence of antibodies indicated that two bsAbs resulted in less selective pressure and could efficiently bind to all single parental mAb-escape mutants. Furthermore, epitope analysis of the protective mAbs against SFTSV and RVFV indicated that they are all located on the Gn subdomain I, where may be the hot spots in the phlebioviruses. Collectively, these data provide potential therapeutic agents and molecular basis for the rational design of vaccines against SFTSV infection.

bunyavirus | SFTSV | glycoproteins | bispecific antibody | structural basis

Severe fever with thrombocytopenia syndrome (SFTS) is an emerging tick-borne infectious disease, resulting in severe clinical symptoms of hemorrhagic fever, encephalitis, and multiple organ failure (1–3). This disease has been reported in China, South Korea, Japan, and Vietnam with a fatality rate of 5 to 30% (1, 4, 5). However, there is currently no vaccine or antiviral therapy available. Although ribavirin exhibits inhibition on SFTSV replication in vitro and in a mouse model, it displayed less effect in a retrospective cohort of patients (4). Favipiravir (T-705), an RNA-dependent RNA polymerase inhibitor of a broad spectrum of RNA viruses, has shown a higher antiviral efficacy for inhibiting SFTSV replication in vitro or in animal models than ribavirin (6). However, large-scale clinical trials need to be conducted to fully establish its safety and efficacy.

SFTS virus (SFTSV), which has been officially named *Dabie bandavirus* or *Bandavirus dabieense*, is the pathogen that causes SFTS. It was first discovered in China in 2009 (1). SFTSV is classified as a member of the genus *Bandavirus* in the *Phenuiviridae* family and *Bunyavirales* order. Its genome contains three RNA segments (S, M, and L) that encode a nucleoprotein, nonstructural protein, envelope glycoprotein, and RNA-dependent RNA polymerase (1). The M segment encodes the precursor of the glycoprotein, which can be further cleaved into Gn and Gc proteins. These two glycoproteins are type I transmembrane proteins. Gn is proposed to be a receptor-binding protein, and Gc is a membrane fusion protein (7–9). Both are critical for SFTSV infection. Rift Valley fever virus (RVFV) and Heartland virus (HRTV) are two pathogens in the genus *Phlebovirus* that cause severe human infectious diseases (10–12). The structures of the Gn head in SFTSV and RVFV have been determined (7, 13). They exhibit similar overall structures, composed of three subdomains. However, the homology and arrangement of the subdomains between these two viruses are not identical. Moreover, the structure of the Gn stem region still needs to be explored.

Monoclonal antibodies (mAbs) targeting glycoproteins represent an effective antiviral strategy against SFTSV. To date, three neutralizing antibodies have been identified (7, 14, 15). MAb4-5 and Ab10 are two neutralizing mAbs screened from a human single-chain variable-region fragment (ScFv) antibody library. Ab10 inhibits SFTSV infection both in vitro and in animal studies, while MAb4-5 exhibits potent inhibition in vitro but displays little protection efficacy in an infected mouse model. A crystal structure shows that the epitope of MAb4-5 is located in subdomain III of the Gn head (7), and alanine scanning indicates that the epitope of Ab10 may be within subdomain II and the stem region of Gn (14). A variable domain of the heavy chain of a heavy-chain antibody (VHH) derived from camel, SNB02,

Significance

Severe fever with thrombocytopenia syndrome virus (SFTSV) is one of the bunyaviruses that caused severe clinical symptoms with a mortality rate ranging from 5 to 30%. Currently, no specific therapeutics or vaccines are available. Neutralizing antibodies targeting viral glycoproteins (Gn and Gc) are potential effective clinical therapeutics. Here, we identified a series of monoclonal antibodies (mAbs) that target these glycoproteins and further developed bispecific antibodies (bsAbs) by analyzing the epitopes of an anti-Gn antibody and an anti-Gc antibody. Our findings revealed that bsAbs demonstrated significantly enhanced neutralization and protection efficacy, surpassing that of parental antibodies both in vitro and in vivo. Furthermore, both protective epitopes of SFTSV and Rift Valley fever virus (RVFV) mAbs located on the Gn subdomain I.

Competing interest statement: Z. Chang, D.G., F.G., and Y.W. are listed as inventors on two pending patent applications. The other authors declare no competing interests.

This article is a PNAS Direct Submission.

[1]Z. Chang, D.G., L.L., and J.S. contributed equally to this work.

[2]To whom correspondence may be addressed. Email: chenzhihai0001@126.com, gaofeng@tib.cas.cn, or wuyan@ccmu.edu.cn.

This article contains supporting information online at https://www.pnas.org/lookup/suppl/doi:10.1073/pnas.2400163121/-/DCSupplemental.

Published June 3, 2024.

fused to a human Fc fragment displays antiviral activity both in vitro and in the mouse model (15). However, both Ab10 and SNB02 only inhibit SFTSV replication after treating mice for 4 d consecutively. Therefore, a more potent protective antibody or an engineered antibody must be developed for clinical treatment, such as a bispecific antibody (bsAb) that combines two antigen-binding sites of two different antibodies within one molecule. This dual-targeting strategy has been proven to hold greater therapeutic efficacy than parental antibodies in cancer and infectious diseases (16–23).

In this study, we identified six human mAbs (SF1, SF5, SF62, SF64, SF71, and SF83) from a SFTS convalescent patient. SF83 bound to Gc, and the other mAbs bound to Gn. Except for the SF62, the other mAbs presented varying neutralizing activities. SF1, SF5, and SF83 exhibit neutralization in both the pseudovirus and the authentic virus systems. Moreover, the crystal structures of antigen–antibody complexes indicate that SF1 binds to the Gn head subdomain III, which is identical to the previously reported MAb4-5 (7). SF5 recognized the Gn head subdomain I, and SF83 bound to Gc domain II. Among these Abs, SF5 presented potent protection in a SFTSV-infected mouse model, and SF83 exhibited partial protection ability. Therefore, we engineered four bispecific antibodies (bsAbs) with DVD-Ig and IgG-$(ScFv)_2$ designs based on this epitope analysis. Two of the bsAbs exhibited synergistic neutralizing ability in vitro, and two others displayed protection efficacy in vivo compared to their parental mAbs. In addition, bsAbs drove fewer escape mutants than mAbs at the same concentration level, which further demonstrates the advantages of bsAbs in the defense of SFTSV.

Results

Screening Anti-Gn/Gc Glycoprotein Antibodies from a Convalescent SFTS Patient. We isolated specific memory B cells from convalescent plasma by using soluble Gn head and Gc proteins as baits. Then, the variable regions of IgG antibodies were determined and cloned into the pCAGGS expression vector as full-length IgG antibodies and were expressed in HEK 293F cells. The six identified antibodies had diverse somatic hypermutation (SHM) rates compared to their germline genes, with nucleotide identities for the variable regions in the heavy chain (V_H) and the light chain (V_L) ranging from 92.5 to 99.7% and 95.8 to 100%, respectively (*SI Appendix*, Table S1). Both the V_H and V_L of antibody SF5 displayed higher identities to the germline gene compared to the other antibodies, with only one SHM in IGVH and no SHM in IGLV (*SI Appendix*, Table S1). In contrast, SF1, SF62, SF64, SF71, and SF83 had lower identities and higher SHM rates than SF5 (*SI Appendix*, Table S1).

The purified mAbs were then tested for Gn/Gc reactivity by enzyme-linked immunosorbent assay (ELISA), with a previously reported Gn-binding mAb, MAb4-5, as a control (Fig. 1 *A* and *B*). Four mAbs (SF1, SF5, SF62, and SF71) bound to Gn, one mAb, SF83, recognized Gc, and SF64 demonstrated no binding to either Gn or Gc (Fig. 1 *A* and *B*). To detect the neutralization properties of the mAbs, we performed neutralization assays using both pseudovirus and authentic virus systems, with MAb4-5 as a control (Fig. 1 *C* and *D*). In the pseudovirus system, SF83 displayed the best neutralizing activity, with a median inhibitory concentration (IC_{50}) value of 3.49 ± 0.38 μg/mL (Fig. 1*C*). SF1, SF5, SF64, and MAb4-5 had 5.3- to 128-fold lower neutralization abilities than SF83 (Fig. 1*C*). In contrast, SF71 displayed much lower neutralization (IC_{50} > 2,400 μg/mL), and SF62 had no neutralization activity at a concentration of 2,400 μg/mL, which is the same as the negative control mAb H4 (Fig. 1*C*). In the authentic virus system, SF83 also exhibited the best neutralization activity among the tested mAbs, with an IC_{50} value of 29.5 ± 12.8 μg/mL (Fig. 1*D*). SF5 and MAb4-5 neutralized the virus with similar IC_{50} values of 73.2 ± 13.8 μg/mL and 65.8 ± 16.8 μg/mL, respectively (Fig. 1*D*). SF1 and SF71

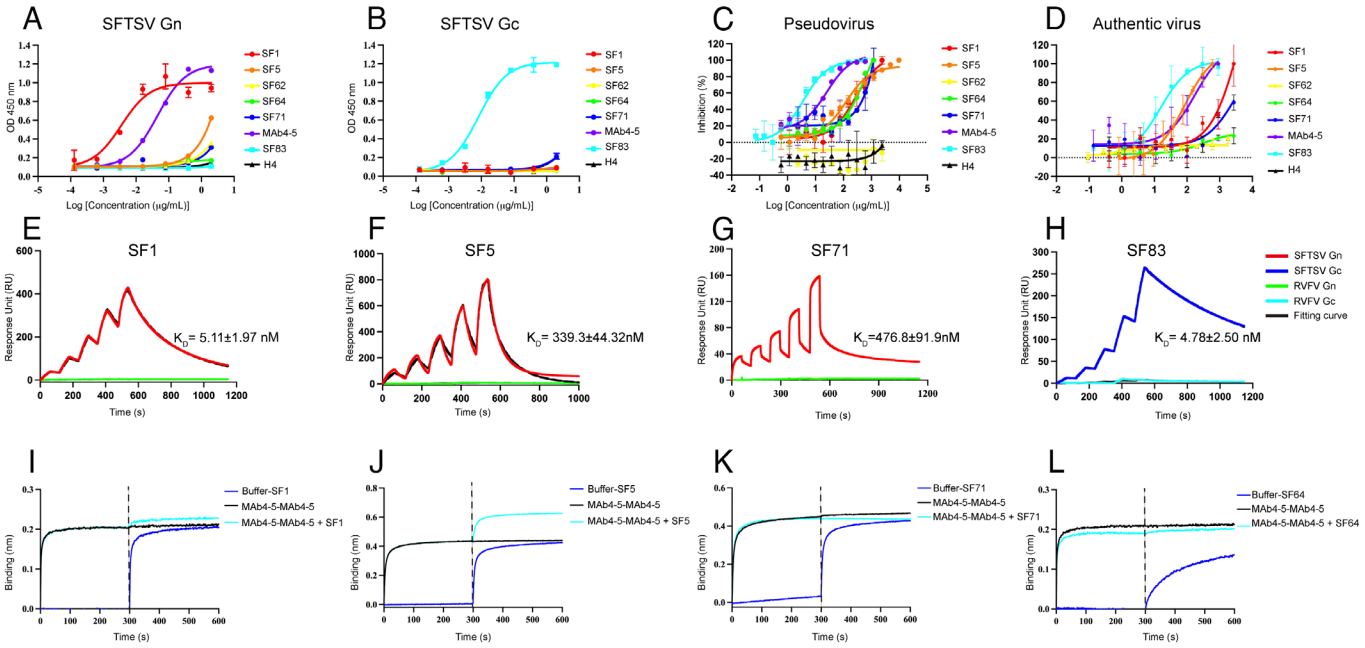

Fig. 1. Screening and characterization of mAbs against SFTSV. (*A* and *B*) Concentration-dependent binding of the mAbs to SFTSV Gn (*A*) or Gc (*B*). (*C*) Concentration-dependent neutralization of pseudovirus by mAbs. (*D*) Concentration-dependent neutralization of authentic SFTSV by mAbs. (*E–H*) Characterization of specific binding between the indicated mAbs and specific antigens, including SFTSV Gn (red), SFTSV Gc (blue), RVFV Gn (green), and RVFV Gc (cyan). The fitting curves are indicated in black lines. The calculated K_D for each mAb binding to the specific antigen is listed accordingly. (*I–L*) Competitive binding to SFTSV Gn between MAb4-5 and another mAb by BLI. Biotinylated SFTSV Gn was immobilized on SA sensors and then saturated with MAb4-5, followed by SF1 (*I*), SF5 (*J*) SF71 (*K*), or SF64 (*L*) in the presence of an equimolar concentration of MAb4-5 (cyan) or without MAb4-5 (black). As a control, the immobilized biotinylated SFTSV Gn was exposed to PBST and then introduced to an equimolar concentration of the indicated mAbs (blue). All ELISAs, neutralization assays, and SPR assays were conducted in at least three independent experiments. The affinity data are represented as the mean ± SD.

displayed relatively lower neutralization (IC_{50} > 2,700 μg/mL) (Fig. 1*D*). In contrast, SF62 and SF64 had no neutralization activity at the highest concentration of 2,400 μg/mL (Fig. 1*D*).

The binding kinetics between antigen and neutralizing mAbs were further evaluated using surface plasmon resonance (SPR) (Fig. 1 *E*–*H*). The antibodies were immobilized on a protein A chip and flowed through SFTSV Gn or Gc protein, with RVFV Gn or Gc as a control. We found that all four mAbs specifically bound to SFTSV antigens, with no binding to RVFV Gn or Gc observed (Fig. 1 *E*–*H*). Moreover, SF1 and SF83 displayed similar binding dynamics with fast K_{on} and slow K_{off} and their binding affinities were at the nanomolar level (5.11 ± 1.97 nM and 4.78 ± 2.50 nM, respectively) (Fig. 1 *E* and *H*). In contrast, SF5 and SF71 exhibited both fast K_{on} and K_{off} and displayed relatively weaker binding affinity for Gn (339.3 ± 44.32 nM and 476.8 ± 91.9 nM, respectively) (Fig. 1 *F* and *G*).

In a previous study, the MAb4-5 epitope was identified, which is located in subdomain III of the SFTSV Gn head. To explore the epitopes of our mAbs targeting Gn, we performed a competition assay using biolayer interferometry (BLI). SF1, SF64, and SF71 competed with MAb4-5, indicating that they share similar epitopes (Fig. 1 *I*, *K*, and *L*). In contrast, SF5 has no competition with MAb4-5, suggesting that these two mAbs recognize different epitopes on the Gn head (Fig. 1*J*).

Structural Basis of Neutralizing mAbs. To identify the precise epitopes of our mAbs, we solved the complex structures of Gn–SF1, Gn–SF5, and Gc–SF83. The complex structures of Gn–SF1 Fab, Gn–SF5 Fab, and Gc–SF83 Fab were determined at resolutions of 2.80, 2.50, and 3.30 Å, respectively (*SI Appendix*, Table S2). These structures indicate that SF1 and MAb4-5 recognize identical epitopes on subdomain III (Fig. 2 *A* and *B*), while SF5 binds to subdomain I (Fig. 2 *A* and *B*). The contact residues between Gn and the antibodies indicate that three regions of the SFTSV Gn head play important roles in the interactions (*SI Appendix*, Tables S3–S5). Sequence analysis of 937 natural SFTSV stains revealed that residues F83 (n = 130), T85 (n = 19), R125 (n = 6), and N170 (n = 102) are the four major positions involved in the interface between Gn and SF5 (*SI Appendix*, Fig. S1). We then performed binding assays using fluorescence-activated cell sorting (FACS) to explore the effect of these naturally occurring mutations. We found that F83 and T85 have partial effects, while N170 has no effect on Gn–SF5 binding (Fig. 2*C*), suggesting that the neutralization of SF5 may be affected by strains carrying F83 or T85 substitutions. Sequence alignment indicated that there are four strains containing a S85 substitution in Gn. However, S85 had no effect on the binding of SF5 to Gn (Fig. 2*C*). Structural analysis revealed that the difference in the side chains between T85 and S85 may be the reason (Fig. 2*C*). Furthermore, we also constructed alanine substitutions of the residues Y83, K125, and D170. We found that Y83A and K125A abolished SF5 binding to Gn, while D170A has no influence on the interaction (Fig. 2*C*). The Gn–SF5 complex structure provides explanations (Fig. 2*C*). Of note, the Y83F substitution retains the stable π–π interactions with P84 and P122, while Y83A disrupts these interactions (Fig. 2*C*). A83 may lead to instability of the 80-loop and 120-loop, thus affecting SF5 binding. The side chain of K125 interacts with D101 and W33 in the heavy chain of SF5 (Fig. 2*C*). Moreover, K125 interacts with both CDR1 and CDR3 of the SF5 heavy chain through a network of water molecules (Fig. 2*C*). Therefore, K125A destroys the hydrophilic environment, thereby losing binding affinity for SF5. We clearly observed that the interactions between D170 in Gn and the residues in SF5 are weak (Fig. 2*C*). Therefore, D170N had no effect on the interaction between Gn and SF5, though D170 can interact with both the heavy chain and light chain of SF5 (Fig. 2*C*).

Previous studies indicate that the Gn proteins of SFTSV and RVFV display similar overall structures (7). However, the epitopes of the currently identified neutralizing mAbs are located on the opposite side of the Gn head (Fig. 2*D*). We superimposed the Gn–SF5 and Gc–SF83 with reported SFTSV Gn–Gc structure (24). We found that the epitope of SF5 is located on the inside of the hexamer/pentamer ring, while most of the MAb4-5/SF1 epitope is exposed on the outside of the ring (Fig. 2*E*). The concealed epitope of SF5 may explain why this mAb has a weaker neutralizing activity than MAb4-5.

To explore the epitope of SF83, we also determined the Gc–SF83 complex structure (*SI Appendix*, Tables S2 and S6), in which domain II and a partial domain I can be observed (Fig. 2*F*). Superimposition of the Gc component of our crystallized Gc–SF83 complex onto a reported SFTSV Gc trimer and a model dimer indicated that the epitope of SF83 is located on the inner side of Gc domain II, which disrupts the assembly of Gc dimers or trimers (Fig. 2 *G* and *H*), suggesting that SF83 neutralizes SFTSV by blocking Gc assembly. Thus far, only the structure of SFTSV Gc in the postfusion conformation has been determined (9). Therefore, we built a model of SFTSV Gc in a prefusion conformation and superimposed the Gn/Gc component of the Gn–mAb and Gc–mAb complexes onto a reported structure of SFTSV Gn–Gc complex (Fig. 2*I*). This revealed that the epitopes of SF5 and SF83 are in proximity (Fig. 2*J*). Therefore, we then designed several bsAbs containing these two parental mAbs.

Engineering bsAbs Targeting Both Gn and Gc. We combined SF5 and SF83 into a single molecule with four different bsAb designs. BsAb1 and bsAb2 were designed as IgG-$(ScFv)_2$, while bsAb3 and bsAb4 were in DVD-Ig format (Fig.3 *A*–*D*). These four bsAbs were produced in FreeStyle™ 293-F cells and purified using protein A chromatography and size-exclusion chromatography (Fig. 3*E*). Then, we performed a competition assay to confirm that epitopes on the bsAbs are accessible to antigens using BLI. The bsAbs were immobilized on Anti-hIgG Fc Capture (AHC) sensors, saturated with Gn or Gc, and then an equal molar mixture of Gn and Gc was flowed in. All of the bsAbs could still bind to the other glycoprotein after saturation with the first glycoprotein, suggesting that both the Gn and Gc binding epitopes on these bsAbs are exposed (Fig. 3 *F*–*I*). To evaluate the binding kinetics of bsAbs to Gn and Gc, we performed SPR assays. We found that all four bsAbs bind to Gn with the same pattern as SF5. The binding affinities are also similar to SF5 (Fig. 3*J*). In contrast, bsAb2 and bsAb4 presented higher binding affinity for Gc, with slow K_{off} and kinetic affinities that exceed the detection range. BsAb1 and bsAb3 displayed similar binding affinities and patterns to SF83, with K_D values of 3.38±0.09 nM and 4.54±0.53 nM, respectively (Fig. 3*J*).

BsAbs Present Enhanced Neutralization Potencies In Vitro, and the Mechanism Was Revealed by the Cryoelectron Microscopy (cryo-EM) Structure of the bsAb3 Fab–Gn–Gc Complex. To determine the neutralizing capacities of the bsAbs, we performed neutralization assays using both pseudovirus and authentic virus systems. In the pseudovirus system, all four bsAbs demonstrated comparable neutralization potencies, with IC_{50} ranges from 0.16 to 0.78 μg/mL (Fig. 4*A*). For SF5 and SF83, the IC_{50} values were 149.1 ± 30.3 μg/mL and 3.49 ± 0.38 μg/mL, respectively, which are much lower than the neutralizing abilities of the bsAbs (Fig. 4*A*). In the authentic virus system, bsAb1, bsAb2, and bsAb3 displayed potent neutralizing activities compared to bsAb4 and the parental mAbs. The IC_{50} values of these three bsAbs ranged from

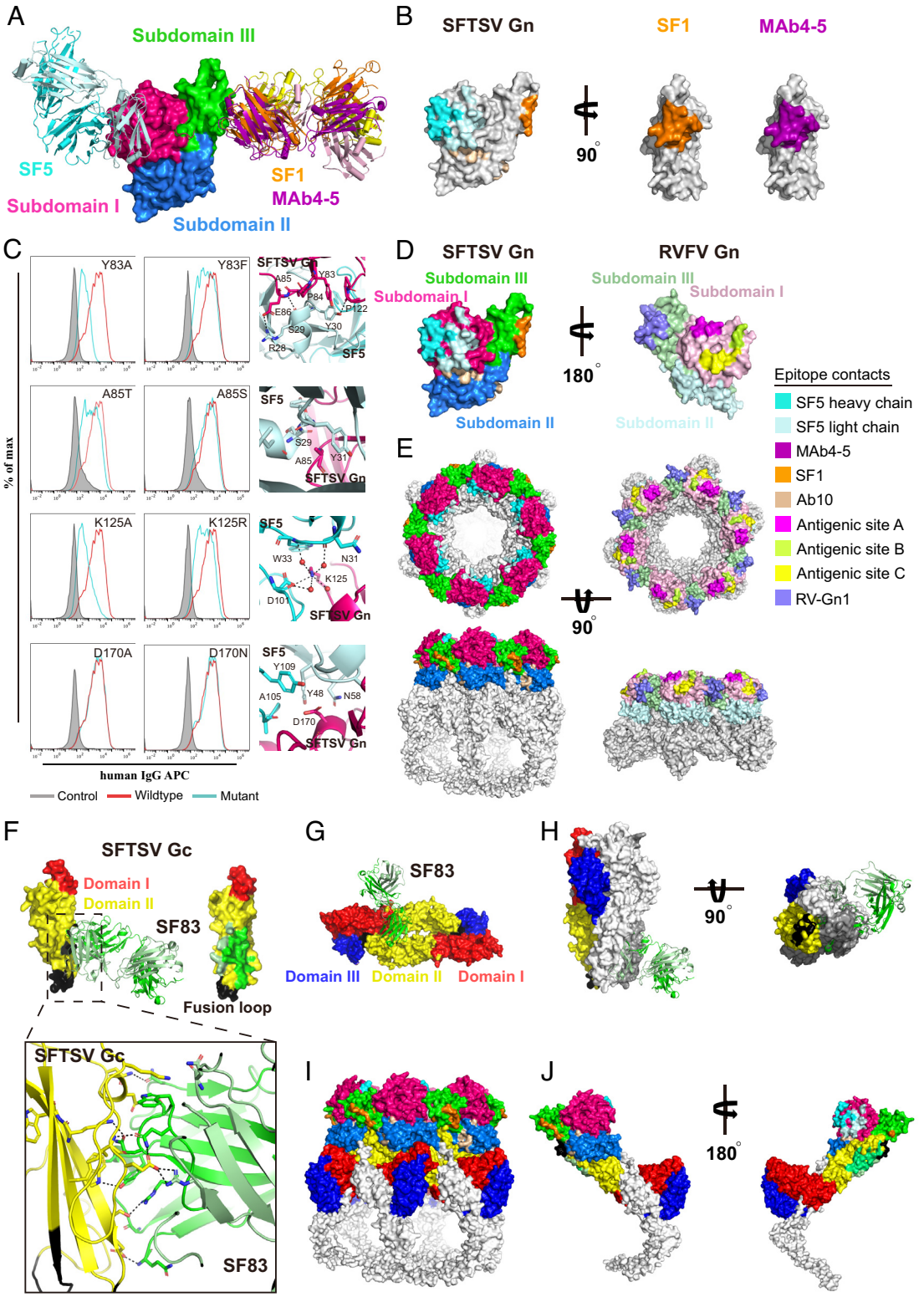

Fig. 2. Structural analysis of the epitopes of SF5 and SF83. (*A*) Superimposition of the Gn–SF1, Gn–SF5, and Gn–MAb4-5 structures. The three subdomains of the Gn head are shown in hot pink, blue, and green, respectively. (*B*) Footprints of SF1 (orange), SF5 (heavy chain in cyan and light chain in light cyan), and Mab4-5 (deep purple) on the SFTSV Gn head. (*C*) Evaluation of the key residues involved in Gn–SF5 binding using a flow cytometric assay. HEK293T cells were transfected with plasmids containing the coding regions of EGFP-fused SFTSV M (red) or the indicated mutants (cyan) and then tested with SF5 and goat anti-human IgG-APC. Cells transiently expressing M-EGFP stained with goat anti-human IgG-APC were used as a negative control (gray). (*D*) Footprints of mAbs on the SFTSV Gn head and RVFV Gn head. SF1 (orange), SF5 (heavy chain in cyan and light chain in light cyan), MAb4-5 (deep purple), and Ab10 (wheat) are mAbs against SFTSV. RV-Gn1 (purple) and mAbs targeting antigenic site A (magenta), B (limon), and C (yellow) recognize the RVFV Gn head. The colors of SFTSV Gn subdomains are consistent with (*A*). The colors of three RVFV Gn subdomains are light pink, pale cyan, and pale green, respectively. (*E*) The indicated RVFV mAbs are superimposed on the Gn–Gc glycoprotein shell of RVFV (PDB code: 6F9E). Four anti-SFTSV Gn mAbs are superimposed on the SFTSV Gn–Gc glycoprotein shell (PDB code: 8ILQ). The *Top* view (*Up* row) and side view (*Bottom* row) are shown. (*F*) Footprint of SF83 and the detailed interactions between SFTSV Gc and SF83. Domains I and domain II of Gc are colored red and yellow, respectively. The heavy chain and light chain of SF83 are green and pale green, respectively. (*G*) Superimposition of Gc–SF83 and the Gc dimer model (constructed based on the RVFV Gc dimer, PDB code: 4HJ1). (*H*) Superimposition of Gc–SF83 and the Gc trimer (PDB code: 6EGU). (*I*) Footprints of mAbs on a SFTSV glycoprotein shell. (*J*) The inner and outer side diagrams of the mAbs' footprints on a Gn–Gc protomer.

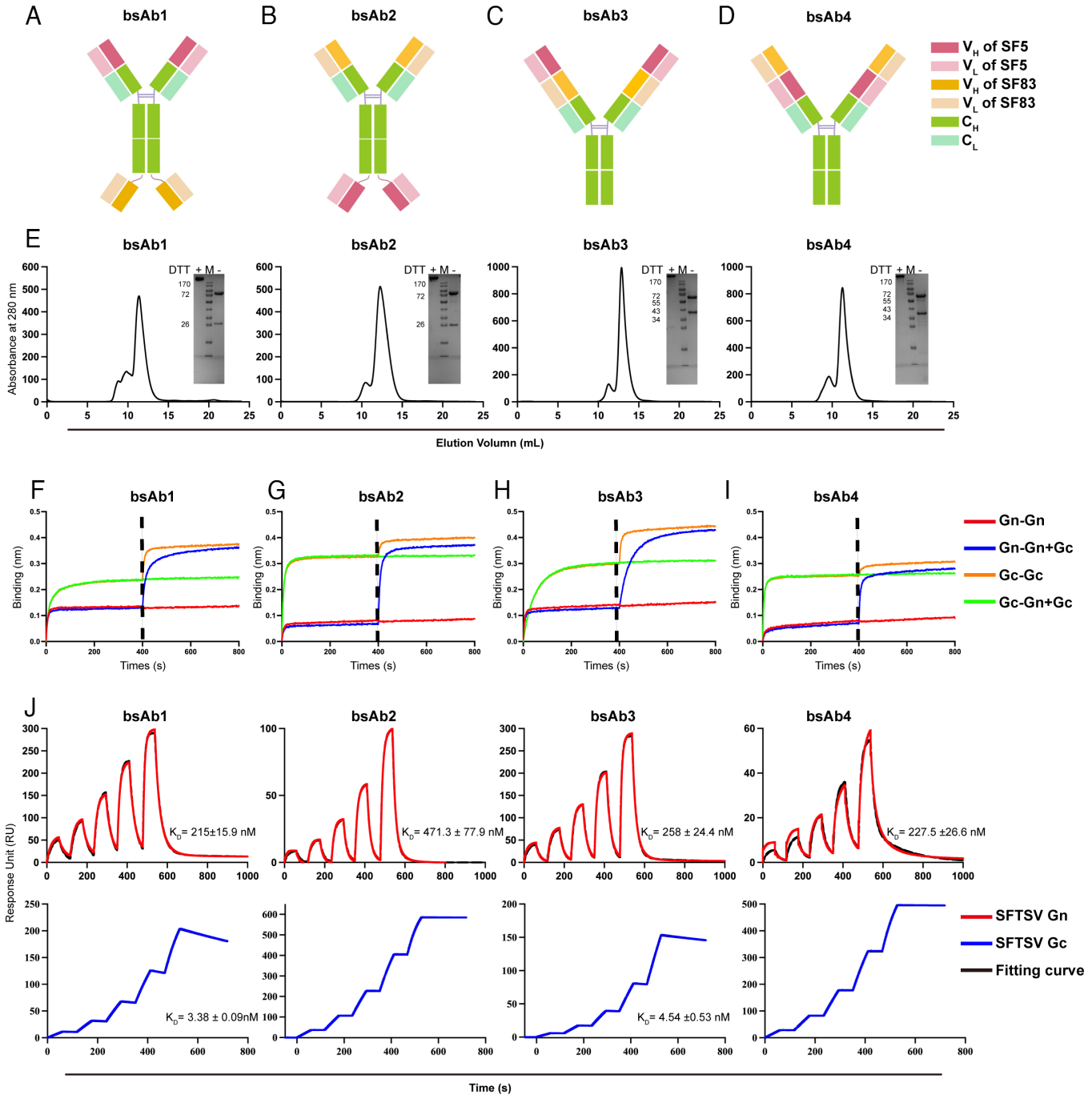

Fig. 3. Design and characterization of bsAbs. (*A–D*) Schematic diagram of four engineering bsAbs. BsAb1 and bsAb2 are in IgG-(ScFv)$_2$ format, whereas bsAb3 and bsAb4 are in DVD-Ig format. (*E*) Size-exclusion analysis of bsAbs. The SDS-PAGE profiles of the pooled samples under reducing and nonreducing conditions. The heavy and light chains of bsAb1 and bsAb2 are ~80 kDa and 25 kDa, respectively. The heavy and light chains of bsAb3 and bsAb4 are ~65 kDa and 40 kDa, respectively. (*F–I*) Competitive binding of parental mAbs and bsAbs. The indicated bsAb was immobilized on the sensor and saturated with Gn, and then flowed through with Gn (red) or an equimolar mixture of Gn and Gc (blue). The indicated bsAb was immobilized on the sensor and saturated with Gc, and then flowed through with Gn (orange) or an equimolar mixture of Gn and Gc (green). The dashed line shows the starting time point of the mixture addition. (*J*) Binding kinetics of bsAbs to SFTSV Gn and Gc. BsAbs were immobilized on Protein A chips and tested for real-time association and dissociation of indicated antigens. The equilibrium dissociation constant (K_D) is labeled accordingly. The solid red line (Gn) and blue line (Gc) are the actual operation curves, and the black line is the fitted curve. Each experiment was repeated three times, and the results shown are the means ± SD.

1.05 to 1.72 μg/mL (Fig. 4*B*). In contrast, the IC_{50} values of bsAb4, SF5, and SF83 were 27.50 ± 1.82, 73.19 ± 13.83, and 29.45 ± 12.80 μg/mL, respectively (Fig. 4*B*). Taken together, bsAb1, bsAb2, and bsAb3 demonstrated better neutralizing potencies than the parental mAbs against both pseudovirus and authentic virus. Furthermore, we also measured the binding abilities of bsAbs to SF5-escape mutations, which revealed that the bsAbs retain their binding activity (Fig. 4*C*), suggesting that the SF83 portion of the bsAbs contributes to binding. We screened amino acid mutations on the SF83 epitope and found that there are fewer mutations than on the SF5 epitope (*SI Appendix*, Fig. S2), suggesting that Gc may have less selective pressure. To further explore the neutralization mechanism of bsAbs, we determined the complex structure of the bsAb3 Fab with both SFTSV Gn head and Gc using cryo-EM (*SI Appendix*, Fig. S3). Single particle averaging and 3D reconstruction yielded a 3.65-Å resolution reconstruction

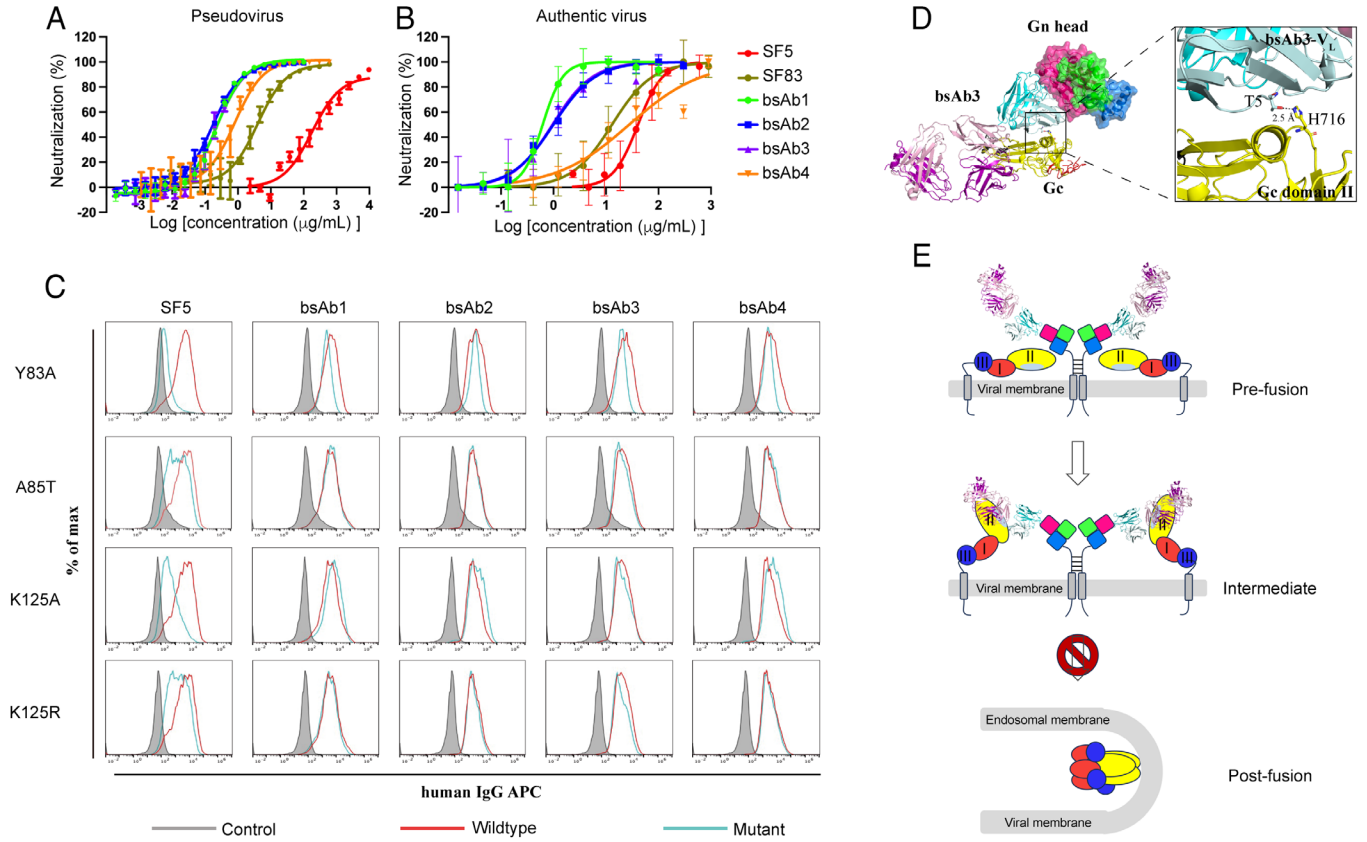

Fig. 4. BsAbs showed potent neutralization against SFTSV and superior binding ability to mutants compared to mAbs. (*A*) Two parental mAbs and four bsAbs were analyzed using the pseudovirus system. (*B*) Two parental mAbs and four bsAbs were analyzed using the authentic virus system. All neutralization assays were conducted in at least three independent experiments. (*C*) Evaluation of the binding abilities between SF5 and bsAbs to different substitutions on Gn using a flow cytometric assay. HEK293T cells were transfected with plasmids containing coding regions of EGFP-fused SFTSV M (red) or indicated substitutions (cyan) and then tested with SF5 or bsAbs and goat anti-human IgG-APC. Cells transiently expressing M-EGFP stained with goat anti-human IgG-APC were used as a negative control (gray). This flow cytometric assay was performed in at least two independent experiments. (*D*) The complex structure of bsAb3 Fab–Gn–Gc and the detailed interaction between SF5 variable regions in bsAb3 and Gc. The Gn head and the variable regions of SF are shown in surface and cartoon representations, with the same color scheme as Fig. 2*A*. Gc is displayed in yellow cartoon format. The heavy chain and light chain of SF83 in bsAb3 are shown in purple and light pink, respectively. The detailed interaction between SF5 and Gc domain II is highlighted in the box. The hydrogen bond between T5 in the bsAb3 light chain and H716 in Gc domain II is labeled with a dashed line. (*E*) Model for bsAb3 neutralization against SFTSV. In the prefusion state, the SF5 on the bsAb3 can bind to Gn subdomain I, while the SF83 epitope is unexposed. At the intermediate state, the Gn and Gc move upward to expose the epitope of SF83, and bsAb3 can bind to both Gn and Gc, thereby preventing Gc trimerization and membrane fusion. The Gn and Gc domains are colored as in Fig. 2*I*, bsAb3 is colored as in (*D*), and the membrane is gray.

of the complex (*SI Appendix*, Table S7). It is clearly observed that the variant region of SF5 can bind to both the Gn head and Gc (Fig. 4*D* and *SI Appendix*, Table S8). The buried surface areas between the variant region of SF5, the Gn head, and Gc are 2376.8 and 795.1 Å^2, respectively. In contrast, the buried surface area between the variant region of SF83 and Gc is 1934.1 Å^2. Moreover, the side chain of H716 in Gc forms a hydrogen bond with the side chain of T5 in the SF5 V_L region of bsAb3 (Fig. 4*D*). Therefore, bsAb3 has more interactions with Gc, which results in a dramatically increased neutralizing ability compared to parental mAbs. Based on this structural analysis, we proposed that bsAb3 binds to the Gn head in the prefusion stage, and then Gc undergoes pH-dependent rearrangements, which drives Gn–Gc dissociation, thereby exposing the epitope of SF83 on Gc domain II. BsAb3 can bind to both Gn and Gc in the intermediate stage, which blocks the fusion process (Fig. 4*E*).

Protection Efficacies In Vivo against SFTSV Infection. In view of the potency and advantages of bsAbs in vitro, we further evaluated their protective efficacies in vivo using type I interferon (interferon α/β) receptor gene knock-out mice. In the preexposure setting, mice were treated with antibodies and administrated 100 $TCID_{50}$ (median tissue culture infectious dose) (50,000 LD_{50}) HB29 after 24 h (Fig. 5*A*). The mortality and body weight change of mice were monitored daily. In the groups treated with 5 mg/kg SF5, bsAb1, or bsAb3, 100% protection was observed (Fig. 5*B*). Treatments of 20 mg/kg SF83 or 5 mg/kg bsAb2 provided partially protection, with survival rates of 40 and 75%, respectively (Fig. 5*B*). In contrast, in the groups of treated with 10 mg/kg SF62 or Mab4-5, all mice died within 7 d (Fig. 5*B*). Mice treated with 10 mg/kg SF83 or 5 mg/kg bsAb4 died within 8 d and 9 d, respectively (Fig. 5*B*).

In the postexposure setting, mice were treated with three different doses of antibodies 24 h after challenge with 100 $TCID_{50}$ HB29 (Fig. 5 *C*–*F*). In the 10 mg/kg treatment group, SF5, bsAb1, and bsAb3 provided 100% protection, bsAb2 and bsAb4 provided 50% protection, and SF83 yielded no protection (Fig. 5*D*). In the 5 mg/kg group, mice treated with bsAb1 or bsAb3 were completely protected, and 80% of mice treated with SF5 survived. However, bsAb2 or bsAb4 presented no protection (Fig. 5*E*). In the 2.5 mg/kg group, bsAb1 and bsAb3 protected 40% of mice from death. In contrast, SF5 displayed 25% protection (Fig. 5*F*). Moreover, we evaluated the protection potency of antibodies in the delayed treatment models (Fig. 5 *G* and *I*). All mice survived in the groups treated with 10 mg/kg SF5, bsAb1, or bsAb3 2 days or 3 days postinfection (d.p.i.) (Fig. 5 *H* and *J*).

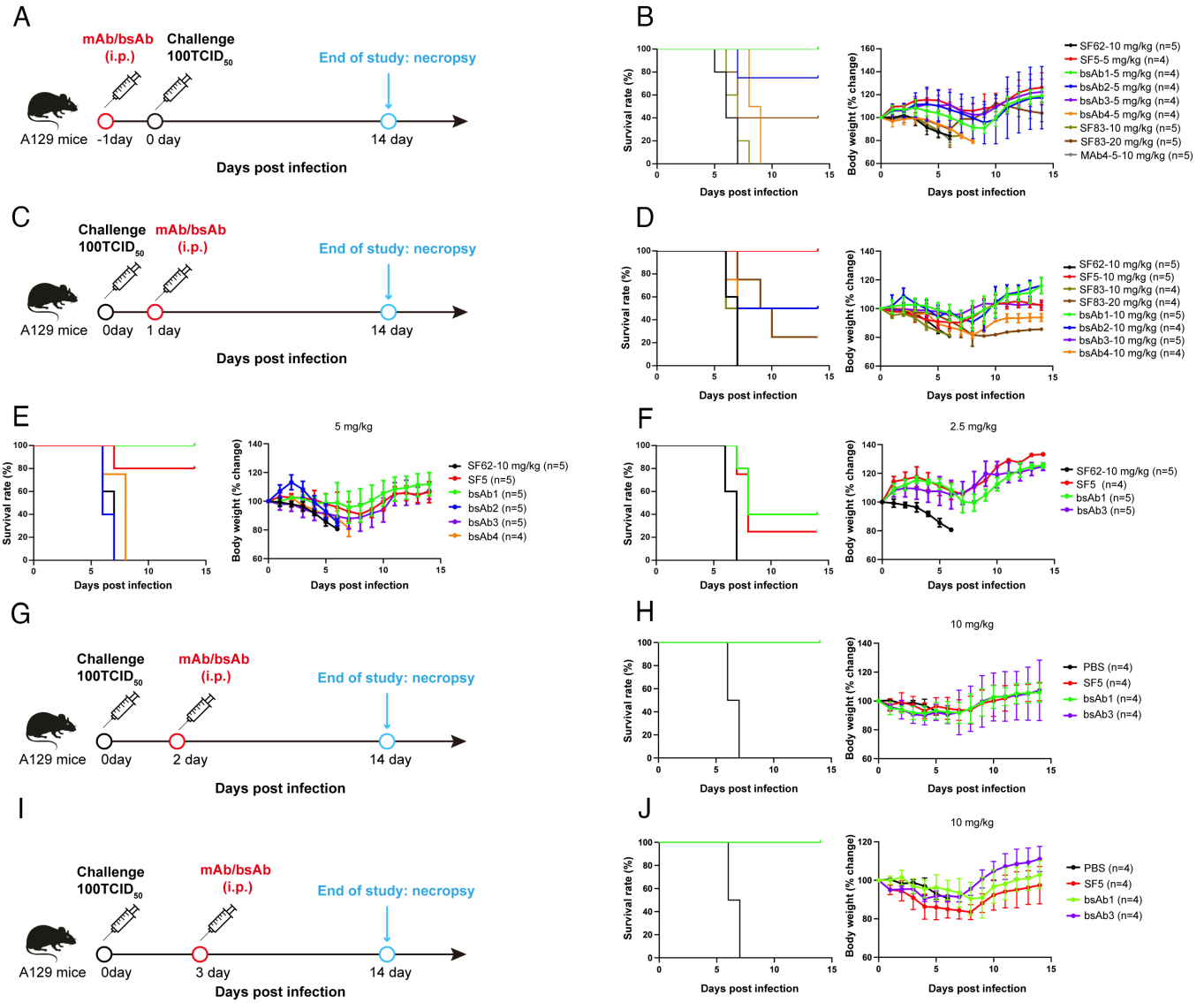

Fig. 5. Prophylactic and therapeutic efficacies of the mAbs and bsAbs in a mouse model of SFTSV infection. (*A*) The prophylaxis strategy of mAbs and bsAbs in the SFTSV-infected A129 mouse model. (*B*) Mouse survival and body weight in the prophylaxis study were recorded daily. Mice in the SF62 group were set as an isotype control. (*C*) The therapeutic strategy of mAbs and bsAbs in the SFTSV-infected A129 mouse model. (*D–F*) Mouse survival and body weight in the therapeutic study were recorded daily. Three doses were used for the therapeutic study, with 10 mg/kg (*D*), 5 mg/kg (*E*), and 2.5 mg/kg (*F*). Mice in the SF62 group were set as an isotype control. (*G* and *I*) The delayed treatment strategies of mAbs and bsAbs in the SFTSV-infected A129 mouse model. Mice were challenged with SFTSV and then were given the indicated antibodies in 2 d (*G*) or 3 d (*I*). (*H* and *J*) Mouse survival and body weight in the delayed treatment study were recorded daily. Mice in the PBS group were administered PBS instead of the indicated antibodies.

Escape Mutant Screening of the mAbs and bsAbs. To evaluate the mutation of SFTSV in the presence of mAbs or bsAbs, we performed escape mutant screening using a vesicular stomatitis virus (VSV)–based pseudovirus system (rVSV-GFP ΔG*M). The ratio of fluorescence values in the antibody-containing well and no-antibody well was monitored. The supernatants in the wells with ratios exceeding 30% were collected for passage. We observed that the concentration of SF5 or SF83 required for inhibiting virus replication increased in the third passage compared to the first passage, and the ratio of the fluorescence value of the indicated wells was >30% (Fig. 6 *A* and *B*), suggesting that escape mutations occurred. In contrast, the ratio of the fluorescence value in all bsAb1- or bsAb3-containing wells was <30%, and no shift was observed in bsAb passage (Fig. 6 *A* and *B*), suggesting that bsAb treatment may not result in an escape mutation at the concentrations used. Therefore, we collected the supernatants from the wells containing the lowest concentration (9.38 μg/mL) of bsAb for the next passage. We then performed next-generation sequencing (NGS) analysis for the first and the third passages of the viruses in the corresponding wells and set wells without antibodies as a control. NGS data analysis indicated that the percentage of four substitutions, A85D, E151K, K710R, and K844T, displayed an increasing trend with passage number under the antibody selection pressure (Fig. 6*C*). A85D and E151K are two substitutions observed in the presence of SF5, found in 93.3% and 51.3% of sequencing reads in the third passage (Fig. 6*C*). In contrast, K710R and K844T are two substitutions observed under the selection of SF83, found in 99.4% and 97.4% of sequencing reads in the third passage (Fig. 6*C*). No dominant substitutions were observed in the presence of bsAbs or the control groups (Fig. 6*C*). Furthermore, we evaluated the binding ability of corresponding antibodies to the dominant substitutions using FACS. The FACS data indicated that A85D and E151K reduce the binding between SF5 and Gn, while the K710R substitution decreased the binding between SF83 and Gc (Fig. 6*D*). In contrast, the binding of bsAbs to these mutants was

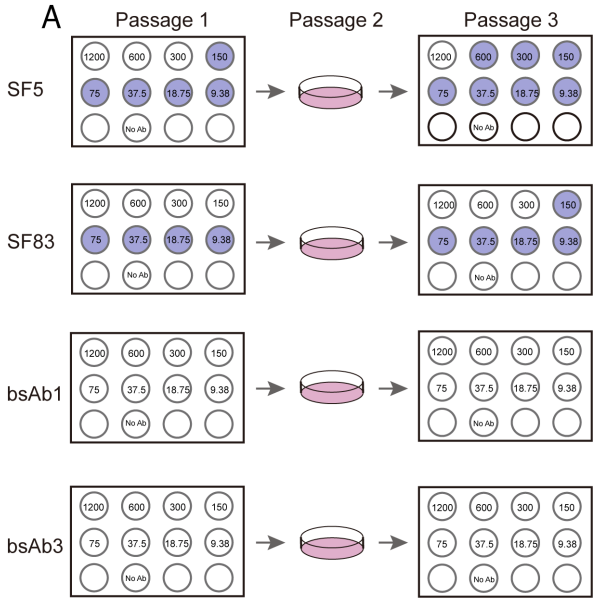

B

	mAbs (μg ml^{-1})	1200	600	300	150	75	37.5	18.75	9.38
Passage 1	SF5	12.2%	23.4%	28.7%	86.4%	82.8%	56.4%	100%	100%
	SF83	<1%	<1%	7.1%	16.0%	45.4%	100%	100%	100%
	bsAb1	<1%	<1%	<1%	<1%	<1%	<1%	<1%	1.3%
	bsAb3	<1%	<1%	<1%	<1%	<1%	<1%	<1%	5.8%
	No Ab	100%	100%	100%	100%	100%	100%	100%	100%
Passage 3	SF5	<1%	34.2%	100%	100%	100%	100%	100%	100%
	SF83	<1%	<1%	10.8%	100%	100%	100%	100%	100%
	bsAb1	<1%	<1%	<1%	<1%	<1%	<1%	<1%	<1%
	bsAb3	0%	0%	0%	<1%	<1%	<1%	<1%	<1%
	No Ab	100%	100%	100%	100%	100%	100%	100%	100%

C

	Position in M gene	254	451	2129	2531
	Reference nucleotide	C	G	A	A
	Variant nucleotide	A	A	**G**	C
	Position in M protein	**85**	**151**	**710**	**844**
	Reference residue	A	E	**K**	K
	Variant residue	D	K	**R**	T
Passage 1	SF5 150 μg ml^{-1}	2.3%	8.4%	<1%	1.1%
	SF83 75 μg ml^{-1}	<1%	<1%	15.5%	47.3%
	bsAb1 9.38 μg ml^{-1}	<1%	<1%	<1%	<1%
	bsAb3 9.38 μg ml^{-1}	<1%	<1%	1.4%	<1%
Passage 3	SF5 600 μg ml^{-1}	93.3%	51.3%	<1%	1.3%
	SF83 150 μg ml^{-1}	1.0%	<1%	99.4%	97.4%
	bsAb1 9.38 μg ml^{-1}	<1%	<1%	<1%	<1%
	bsAb3 9.38 μg ml^{-1}	<1%	<1%	<1%	<1%
	No Abs WT	<1%	<1%	<1%	<1%

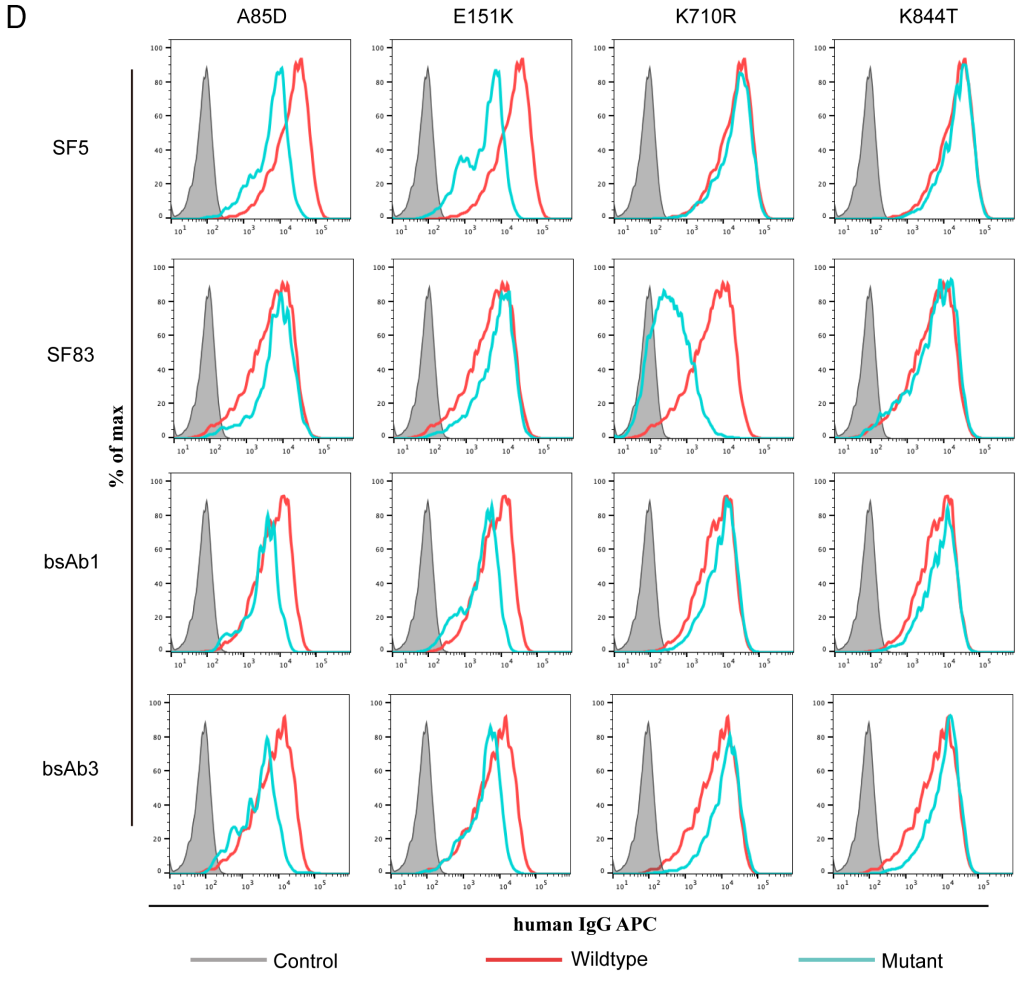

Fig. 6. Escape mutant screening in the presence of antibodies. (*A*) Schematic of the escape mutant screening process. The VSV-GFP-based pseudovirus was passaged in the presence of antibodies with serial dilutions on Vero E6 cells. The light purple indicates the fluorescence value ratio in the indicated well and no-antibody well was >30%. The corresponding ratio values are indicated in (*B*). (*B*) Quantitative percentage of infected cells (monitored by transducing units) under different concentrations of antibodies during passage 1 and passage 3. Yellow boxes indicate the dilutions that were passaged and sequenced in passage 1 or passage 3. (*C*) NGS of virus genomes from passage 3. Variant nucleotides and corresponding residues are listed, and the qualitative percentage of infected cells (monitored by transducing units) was calculated (dark purple, >60%; pink, 30 to 60%; and light purple, 10 to 30%). (*D*) Evaluation of the binding between SF5, SF83, and bsAbs to screened substitutions using a flow cytometric assay. HEK293T cells were transfected with plasmids containing coding regions of EGFP-fused SFTSV M (red) or the indicated substitutions (cyan) and then tested with SF5, SF83, or bsAbs and goat anti-human IgG-APC. Cells transiently expressing M-EGFP stained with goat anti-human IgG-APC were used as a negative control (gray).

barely impaired, suggesting the advantages of bsAbs in preventing immune escape (Fig. 6*D*).

Discussion

SFTSV causes SFTS with a fatality rate of 5 to 30% (1, 4, 5). However, there are currently neither registered preventive vaccines nor effective therapeutics available. In this study, we identified several mAbs that target glycoproteins on the SFTSV. Among these mAbs, SF5 and SF83 bound to Gn and Gc, respectively, and exhibited neutralization in vitro and protective abilities against SFTSV in a mouse model. We also identified their epitopes by determining the antigen–mAb complex structures and further developed bsAbs in both IgG-$(ScFv)_2$ and DVD-Ig formats based on epitope analysis. Two bsAbs displayed improved potency both in vitro and in vivo. The mechanism of DVD-Ig was revealed by determining the bsAb3 Fab–Gn–Gc complex structure using cryo-EM. Moreover, bsAbs drive less selective pressure compared to parental mAbs, suggesting the advantages of their clinical use in the future.

In previous studies, two SFTSV-protective antibodies were reported with A129 mice or NCG-HuPBL mice, respectively (14, 15). However, these two antibodies only display protection when administered to mice for four consecutive days. Moreover, the dosage required is 600 μg/day (30 mg/kg Ab10) or 400 μg/day, respectively. In contrast, 10 mg/kg SF5 and 5 mg/kg bsAb1 or bsAb3 provided complete protection with one dose in our study here. Furthermore, 5 mg/kg of bsAb1 and bsAb3 provided 100% protection with one dose, which further proves the potency of these bsAbs. In our study, an A129 mouse model was used to evaluate the protective efficacy of the antibody. Considering the differences between humans and mice, the SF5 and bsAbs should be further evaluated in a nonhuman primate model in the future.

Antibodies play an essential role in protection against virus infections (21, 25–27). Some of them can prevent viral entry into cells or induce lysis of infected cells through antibody-dependent cellular cytotoxicity (ADCC) or complement-dependent cytotoxicity (CDC) (28). The ADCC and CDC effects of SF5, bsAb1, and bsAb3 should be further explored. With its lower SHM rates in both heavy chain and light chain, SF5 has a relatively low binding affinity for SFTSV Gn, with both a fast association rate and disassociation rate. However, this mAb shows potent protective efficacy in a SFTSV infection mouse model. Therefore, several approaches can be applied to improve the affinity of SF5. On one hand, a random substitution library should be constructed and screened. One the other hand, structure-based SF5 modification could be performed. Moreover, more mAbs have been identified against SARS-CoV-2 and influenza virus than bandaviruses. Further screening mAbs targeting this epitope from convalescent patients may also uncover potent protective mAbs with high affinity. SF83 exhibits high affinity in vitro but lower protective efficacy in vivo. The reason may be that purified Gc protein using in the binding affinity is a monomer, and the SF83 epitope is exposed, thereby displaying high affinity. However, the SF83 epitope located in the inner side of Gc domain II when superimposed the SF83 into the SFTSV glycoprotein architecture. A similar situation may happen in vivo that the SF83 epitope may be exposed when the conformation changed; therefore, the protective efficacy is low.

BsAbs offer advantages in neutralizing activities and spectrum against severe acute respiratory syndrome coronavirus 2 and HIV-1 (16, 17, 21, 22). DVD-Ig and IgG-$(ScFv)_2$ are two formats that can increase neutralizing activity in vitro and therapeutic efficacy in vivo. However, our results in this study indicated that the construction order of the parental mAb in bsAbs plays important roles in neutralization and protection effects of bsAbs. Both bsAb1 and bsAb3 were constructed with the SF5 variable region at the N terminus, which synergistically increased the neutralizing activity and therapeutic efficacy. In contrast, bsAb2 and bsAb4, which have the SF83 variable region at the N terminus, displayed less potent therapeutic efficacy. Intriguingly, bsAb2 and bsAb4 presented different neutralizing abilities against authentic virus, which indicates that the DVD-Ig design neutralizes virus better than the IgG-$(ScFv)_2$ design. This mechanism needs to be further investigated.

Both SFTSV and RVFV belong to the *Phenuiviridae* family in different genera. Previous studies demonstrate that their glycoproteins display similar overall structures, though they have low sequence identity (7). The epitopes of RVFV-protective mAbs are mainly located at the RVFV Gn head subdomain I (25), which is exposed on the outer surface. In this study, the mAb SF5 recognized a cryptic epitope on the SFTSV Gn head subdomain I when we superimposed the SF5-Gn structure onto a SFTSV structure. Moreover, the RVFV Gn–Gc complex reveals that Gn shields the Gc fusion loop to keep it in the prefusion state, and Gc forms a kinked conformation rather than a class II fusion protein structure observed in crystallographic investigations (13). Our study here, with other RVFV reports, implies that the mAb protection mechanism in different bunyaviruses could be different.

Materials and Methods

Antigen-Specific mAb Selection from a Convalescent Patient. A blood sample from a convalescent patient was collected under study protocols approved by Beijing Ditan Hospital, Capital Medical University. The donor provided written informed consent for the use of blood and blood components. Peripheral blood mononuclear cells (PBMCs) were isolated and then subjected to cell sorting as previously reported (25, 26). Briefly, PBMCs were incubated with both purified His-tagged Gn and His-tagged Gc at 100 nM on ice for 30 min. After being washed with PBS (phosphate-buffered saline) three times, PBMCs were stained with mouse anti-human Allophycocyanin (APC)/cyanine7 CD19, APC mouse anti-human CD38, Pacific blue mouse anti-human CD27, Plycoerythrin (PE)/cyanine5 mouse anti-human CD3, PE/cyanine5 mouse anti-human CD235a, PE/cyanine5 mouse anti-human CD16, PE mouse anti-His, and Fluorescein (FITC) mouse anti-human IgG (hIgG) antibodies. Antigen-specific memory B cells ($CD19^+$, $CD27^+$, $hIgG^+$, $CD235a^-$, $CD16^-$, $CD3^-$, $CD38^-$, and His^+) were sorted into 96-well PCR plates with one cell per well on a BD FACSAriaIII flow cytometer (BD Biosciences), and the data were analyzed using FlowJo v10.8 (BD Biosciences). The cDNAs of IgV_H and IgV_L chains were amplified by reverse transcription, and then the DNAs of these chains were amplified using two rounds of PCR. Sequences were analyzed using the International ImMunoGeneTics information system to identify the variable regions and somatic mutations.

Construction, Protein Expression, and Purification. The SFTSV Gn head domain (residues 20 to 340, GenBank accession number JF906057.1), SFTSV Gc ectodomain (residues 563 to 995, GenBank accession number. JF906057.1), RVFV Gn head domain (residues 154 to 469, GenBank accession number JQ068143.1), and soluble RVFV Gc (residues 691 to 1,118, GenBank accession number JQ068143.1) followed by a C-terminal six-histidine tag were subcloned into pCAGGS with an IL-2 signal sequence at the N terminus, respectively. These glycoproteins were expressed in 293F cells and purified by affinity chromatography using a HisTrap High-Performance column (GE Healthcare) and by size-exclusion chromatography using a Superdex 200 10/300 increase column.

The genes of the IgV_H regions were cloned into the modified pCAGGS with an Ig leader sequence at the 5′ end and a heavy chain constant region at the 3′ end. The genes of the IgV_L regions were then cloned into modified pCAGGS with an Ig leader sequence at the 5′ end and a kappa chain or a lambda chain constant region at the 3′ end. The mAbs were expressed in 293F cells by cotransient transfection of both heavy chain and light chain plasmids. The mAbs were then purified using a HiTrap Protein A column (GE Healthcare), followed by size-exclusion

chromatography using a Superdex 200 10/300 increase column (GE Healthcare). To generate mAb Fabs, the mAb IgGs were digested with immobilized papain (Thermo Scientific) according to the manufacturer's instructions and then purified using a HiTrap protein A column (GE Healthcare).

The DVD-Ig and IgG-$(ScFv)_2$ designs of the bsAbs were constructed as described in a previous study (21). Briefly, for the DVD-Ig format, the two different IgV_H regions were fused with a $(G_4S)_2$ linker and followed with a heavy chain constant region at the 3′ end. For the light chain, the two different IgV_L regions were fused with a $(G_4S)_2$ linker and followed with a light chain constant region at the 3′ end. For the IgG-$(ScFv)_2$ design, a ScFv of one mAb was connected to the C terminus of another mAb heavy chain with a GGS linker. The light chains were paired with the corresponding heavy chains. The expression and purification of the bsAbs were the same as for the mAbs described above.

ELISA. First, 100 ng of recombinant SFTSV Gn or Gc proteins were coated on the 96-well half-area microplates (3590, Corning) at 277 K overnight, and then blocked with 5% goat serum for 1 h at room temperature. After washing with PBST (0.05% Tween-20 in PBS) three times, 100 μL of 10-fold serial dilutions of the convalescent patient's plasma were added to each well and incubated for 1 h. Then, the plates were washed with PBST three times and incubated with horseradish peroxidase (HRP)-conjugated anti-human Fc antibody (80794111, Easybio) for 30 min. The plates were washed with PBST three times, and each well received 50 μL of 3,3′,5,5′-tetramethylbenzidine (TMB) substrate solution (P0209, Beyotime). The reaction was stopped by adding 50 μL of 2 M sulfuric acid. The absorbance of each well was measured at 450 nm using a microplate spectrophotometer (Thermo Scientific).

Flow Cytometry. The plasmids of pEGFP-SFTSV M, or pEGFP-SFTSV M mutants (Y83A, Y83F, A85S, A85T, A85D, K125A, K125R, E151K, D170A, D170N, K710R, and K844T) were transfected into HEK293T cells. At 48 h posttransfection, cells were collected and stained with the SF5, SF83, or bsAbs at a concentration of 50 μg mL^{-1}, 4 μg mL^{-1}, and 5 μg mL^{-1} for 30 min, respectively. The cells were then washed with PBS and stained with anti-human IgG-APC. The cells were subjected to analysis using a BD FACSCalibur. Data were analyzed by FlowJo v10.8 (BD Biosciences).

SPR Analysis. The affinities between SFTSV Gn head or Gc proteins and antibodies were measured at room temperature using a BIAcore 8K system. Antibodies were immobilized on protein A chips and flowed through with serially diluted SFTSV Gn head/Gc. All proteins used for kinetic analyses were dialyzed against PBST buffer. A twofold dilution of SFTSV Gn head/Gc was then flowed over the chip surface. After each cycle, the chip surface was regenerated with Gly-HCl, pH 1.5. A two-state reaction model for bsAbs and a 1:1 binding model for mAbs were used to analyze the data with Biacore evaluation software.

Competition Assay. To identify the epitopes on the bsAbs, we immobilized the bsAbs on AHC sensors saturated them with 400 nM SFTSV Gn head or Gc, and then flowed through with 400 nM Gn head and Gc mixtures. The binding signal indicated that bsAbs bind to both Gn and Gc. To determine the epitopes of the mAbs (SF1 and SF5) targeting the Gn head, the SA sensors were immobilized with biotin-labeled SFTSV Gn head proteins and then saturated with the first mAb. After the binding curve reached saturation, it confirmed that the Gn was occupied by the first mAb. Subsequently, the sensors were loaded with the mixture of the first mAb and the second mAb. The binding signal indicated whether the mAb epitopes overlapped or not.

Pseudovirus-Based and Authentic Virus Neutralization Assays. For pseudovirus-based neutralizing assays, Vero E6 cells were seeded in 96-well plates 12 h prior to infection. The antibodies were twofold serially diluted, and 50 μL of the VSV-based pseudovirus system (rVSV-GFP ΔG*M) was added at 1,000 to 2,000 TU/well (transducing units/well) and incubated with diluted antibodies at 37 °C for 1 h. The mixtures were then added to preplated Vero E6 cells and incubated at 37 °C for 12 h. Then, TU numbers were monitored using a CQ1 confocal image cytometer (Yokogawa). Each sample was tested in triplicate. Wells without antibodies were used as controls.

For authentic virus-neutralizing assays, Vero E6 cells were seeded in 96-well plates at 12 h prior to the infection. The antibodies were threefold serially diluted, 50 μL of 200 $TCID_{50}$ HB29 was incubated with 50 μL of diluted antibodies at 37 °C for 2 h, and then the supernatant was replaced with 100 μL of 2% Fetal Bovine Serum Dulbecco's Modified Eagle's Medium (DMEM) and cultured at 37 °C for 48 h. Next, the culture medium was removed, and the cells were fixed with a cold 1:1 methanol-ethanol solution at −20 °C for 12 h. The plate was washed with PBST and blocked with 5% skim milk for 2 h at room temperature. Then, the plate was washed with PBST and stained with MAb4-5 or SF83, which was diluted to 1 μg/mL for 2 h. Cells were washed with PBST and incubated with goat anti-human IgG HRP (Easybio) for 1 h. The plate was then washed with PBST and developed with TMB substrate for 10 to 15 min. The reaction was stopped with 2 M hydrochloric acid, and the absorbance of each well was measured at 450 nm using a microplate spectrophotometer (Thermo Scientific).

In Vivo Protection Assay. Twenty-five randomly assigned 6- to 8-wk-old A129 mice were divided into five groups to determine the median lethal dose (LD_{50}) of SFTSV infection. Four groups of mice were challenged subcutaneously with the indicated $TCID_{50}$ of SFTSV isolate HB29, and one group was injected with PBS as a control. All of the mice were then monitored daily for survival and body weight for 14 d.

In the prophylaxis assays, groups of four (for mAbs SF5, bsAb1, bsAb2, bsAb3, and bsAb4) or five (for mAbs SF83 and MAb4-5) randomly assigned A129 mice were treated with the indicated mAbs or PBS and challenged subcutaneously with 100 $TCID_{50}$ (50,000 LD_{50}) 24 h later. In the treatment assays, groups of four or five randomly assigned A129 mice were challenged subcutaneously with 100 $TCID_{50}$ (50,000 LD_{50}) at 24 h prior to being treated with the indicated mAbs or PBS. In the delayed treatment models, randomly assigned A129 mice were challenged subcutaneously with 100 $TCID_{50}$ (50,000 LD_{50}) at 48 h or 72 h prior to being treated with the indicated mAbs or PBS. All mice were monitored daily for survival and body weight for 14 d.

Crystallization, Data Collection, and Structure Determination. SFTSV Gn head and the indicated Fabs were mixed at a molar ratio of 1:1 and incubated at 277 K for 1 h. The mixture was then purified on a Superdex 200 10/300 increase column in 20 mM Tris, pH 8.0, and 50 mM NaCl. The Gn head–Fab complex was pooled and concentrated to 10 mg mL^{-1} for crystallization. All crystallizations were performed using the vapor-diffusion sitting-drop method with 1 μL protein mixed with 1 μL reservoir solution. The crystals of the Gn head–SF1 complex were observed in the reservoir solution composed of 0.2 M potassium bromide, 0.2 M potassium thiocyanate, 0.1 M sodium cacodylate, pH 6.5, 3% (w/v) γ-PGA (Na+ form, LM), and 30% (v/v) polyethylene glycol (PEG) 400 at 291 K. The crystals of the Gn head–SF5 complex were observed in the reservoir solution composed of 0.1 M 2-morpholinoethanesulfonic acid monohydrate, pH 6.0, and 14% (w/v) polyethylene glycol 4000 at 291 K. The crystals of the Gc–SF83 complex were observed in the reservoir solution composed of 0.1 M Tris, pH 7.8, 5% (w/v) γ-PGA (Na+ form, LM), and 15% (w/v) PEG 4000 at 291 K. Crystals were frozen in liquid nitrogen in reservoir solution supplemented with 20% glycerol (v/v) as a cryoprotectant. Data were collected at the Shanghai Synchrotron Radiation Facility. All data were processed with HKL2000 (29). The structures of Gn–SF1, Gn–SF5, and Gc–SF83 complexes were determined by molecular replacement using SFTSV Gn (5Y10) or Gc (5G47) as models. The atomic models were completed with COOT (30) and refined with PHENIX (31).

Cryo-EM Sample Preparation and Data Acquisition. To prepare the cryo-samples, the bsAb3 Fab–Gn–Gc complex sample was vitrified using a Vitrobot Mark IV (ThermoFisher Scientific) plunge freezing device. The sample (4 μL, 1 mg mL^{-1}) was applied to Au Quantifoil 1.2/1.3 holey carbon grids that were glow discharged for 40 s. The grids were then blotted using different conditions (blot time 2 s and blot force 0; blot time 3 s and blot force −4) at a temperature of 4 °C and a humidity level of >99% and plunge frozen into liquid ethane. The prepared grids were transferred to a 300 kV Titan Krios transmission electron microscope equipped with a Gatan K3 detector and a GIF Quantum energy filter. Movies were collected at 105,000× magnification with a calibrated pixel size of 0.69 Å over a defocus range of −1.0 μm to −2.0 μm in superresolution counting mode with a total dose of 60 $e^-/Å^2$ using EPU (ThermoFisher Scientific) automated acquisition software.

Cryo-EM Image Processing. The detailed data processing workflow is summarized in *SI Appendix*, Fig. S3. All of the raw dose-fractionated image stacks were 2× binned, aligned, dose-weighted, and summed using MotionCor2 (32). The contrast transfer function (CTF) estimation, particle picking and extraction, 2D classification, ab initio

model generation, and 3D refinements were performed in cryoSPARC v.3.3.1 (33). For the bsAb3 Fab–Gn–Gc complex, a total of 9,583 micrographs were collected for this dataset. We picked particles using the blob-pick procedure of cryoSPARC from 500 micrographs, and then these particles were subjected to 2D classification. After three rounds of 2D classification, we selected good particles in different views for Topaz training and then generated the Topaz model. Then, we applied the Topaz (34) procedure to select particles against entire micrographs. The 1,038,267 initial particles were picked and extracted with a box size of 440 pixels from 9,583 micrographs. After extensive 2D classification, approximately 817,688 good particles were selected to generate the initial models, and two rounds of heterogeneous refinement resulted in six distinct volumes. The dominant class containing 26.29% of total particles was identified, which displayed clear features of secondary structural elements. These particles were subjected to nonuniform and CTF refinements in cryoSPARC v.3.3.1, which yielded a final density map at 3.65 Å resolution. The density map was estimated by the gold-standard Fourier shell correlation cut-off value of 0.143 and was sharpened by DeepEMhancer.

Cryo-EM Model Building and Structure Refinement. The structures of the SFTSV Gn–SF5 (PDB 8WSP) and Gc–SF83 (PDB 8WSU) proteins were rigidly docked into the density map using Chimera (35); mutation and manual adjustment were performed with Coot v.0.9.3 (36). Glycans were added at N-linked glycosylation sites in Coot. Each residue was manually checked with the chemical properties taken into consideration during model building. Several rounds of real-space refinement in Phenix-1.20.1 (37) and manually building in Coot were performed until the final reliable models were obtained. Molprobity (38) was used to validate geometry and check structure quality. Statistics associated with data collection, 3D reconstruction, and model building are summarized in *SI Appendix*, Table S7. Figures were generated using Chimera (35) and PyMol v.2.0 (http://www.pymol.org).

Escape Mutant Screening and NGS. Escape mutants were selected in the presence of individual mAbs or bsAbs using the VSV-based SFTSV pseudovirus. The experiments were performed according to the methods reported previously, with some modifications (21). Briefly, the antibodies were serially diluted twofold on a 12-well plate. The concentrations of antibodies ranged from 9.38 to 1,200 μg mL^{-1}. The titers of the VSV-based SFTSV pseudotyped viruses were determined by the transducing units measured by the CQ1 quantitative confocal image cytometer (Yokogawa). An equal volume of diluted virus was then incubated with the diluted antibodies at 37 °C for 1 h. Then, the mixtures were added to 12-well plates of prepared Vero E6 cells at 37 °C for 1 h. The supernatant was discarded, and the cells were washed twice with PBS. After that, 1 mL of DMEM containing the antibodies with the concentration of the corresponding wells was added. The plates were then incubated at 37 °C and monitored using a CQ1 quantitative confocal image cytometer every 24 h for three consecutive days. The supernatant was collected from the wells with the highest antibody concentration with an infection rate >30% (the ratio of sample well value to control well value). For bsAb1 and bsAb3, supernatants were collected from the wells with a concentration of 9.38 μg mL^{-1} because none of the wells had an infection rate >30%. For the second passage, 200 μL of supernatant from the first passage was amplified in a well in a 12-well plate containing Vero E6 cells in the presence of the same antibody concentration. After 16 h, the supernatant was collected, and the titer was determined. For the third passage, 200 μL of supernatant from the second passage was used, and the passaging method was the same as the first one. The infection rate was monitored, and the concentration range shift of antibodies between passage 1 and passage 3 was recorded. Supernatant was collected from the wells with the highest antibody concentration with an infection rate >30%. For bsAb1 and bsAb3, supernatant was collected from the wells with a concentration of 9.38 μg mL^{-1} because none of the cells in the wells had an infection rate >30%. Viral RNAs from the supernatants collected from passage 1 and passage 3 were extracted using the MagaBio plus Virus RNA Purification Kit (BIOER). Reverse transcription PCR was then performed using a HiScript II One Step RT-PCR Kit (Vazeyme) to obtain M segments of the SFTSV pseudoviruses. The specific primers were used as follows: 5′-GCTTCTGAACAATCCCCGGT-3′; and R: 5′-CGATTCCCTCGATGTGGGAT-3′. DNA library preparation was performed using the NGS Fast DNA library Prep Set for Illumina. The RNA-sequencing data were acquired by NGS technology using Illumina NovaSeg 6000. Raw NGS reads were processed by filtering sequence length <50 and base number >6 with fastp software (version 0.20.0). Then, the filtered reads were mapped to the SFTSV by Burrows–Wheeler aligner (BWA version 0.7.17-r1188). SAMtools (version 1.9) was used for SNP calling with default settings. Single-nucleotide polymorphisms with a minimum frequency of 5% were identified and annotated.

Sequence Alignments. We collected a total of 937 SFTSV M genes from the NCBI. These genes were aligned with MUSCLE (v3.8.31) with default parameters (39). The maximum-likelihood (ML) tree was inferred using IQ-TREE2 with 1000 bootstraps (40). The best-fit model of the phylogenetic tree was determined with ModelFinder (41). The phylogenetic tree was visualized with Interactive Tree of Life (iTOL) v5 (42).

Quantification and Statistical Analysis. The results on the binding abilities of mAbs or bsAbs to Gn or Gc are presented as the mean values from three independent experiments. Neutralization titers are presented as the geometric mean of the IC_{50} values calculated using three-parameter logistic regression from three independent experiments. Error bars are defined as the SD. All data were analyzed using Prism software 8.0.

Data, Materials, and Software Availability. The crystal structures of the Gn–SF1, Gn–SF5, and Gc–SF83 complexes were deposited to the PDB with accession codes 8WSN (43), 8WSP (44), and 8WSU (45), respectively. The cryo-EM map and atomic model of the bsAb3 Fab–Gn–Gc have been deposited at the Electron Microscopy Data Bank and the PDB with accession code 8WQW (46). All other data are included in the manuscript and/or *SI Appendix*.

ACKNOWLEDGMENTS. The VSV-based pseudovirus system (rVSV-GFP ΔG*M) was obtained from Prof. Aihua Zheng. We thank all the staff at the Shanghai Synchrotron Radiation Facility beamline BL19U1 and BL02U1. We thank all the staff at the Cryo-EM Center, Shanxi Academy of Advanced Research and Innovation for their operation and maintenance of the cryoelectron microscope. We are grateful to Dr. Zheng Fan in the Institute of Microbiology, Chinese Academy of Sciences, for her assistance with SPR experiments. This work was supported by the National Natural Science Foundation of China (32090014 and 82022042) and the National Key R&D Program of China (2022YFC2303402 and 2020YFA0907104).

Author affiliations: [a]Department of Pathogen Microbiology, School of Basic Medical Sciences, Capital Medical University, Beijing 100069, China; [b]Chinese Academy of Sciences Key Laboratory of Pathogen Microbiology and Immunology, Institute of Microbiology, Chinese Academy of Sciences, Beijing 100101, China; [c]College of Veterinary Medicine, Shanxi Agricultural University, Jinzhong, Shanxi 030801, China; [d]Faculty of Health Sciences, University of Macau, Macau SAR 999078, China; [e]Department of Microbiology, Federal University of Technology, PMB704, Akure, Nigeria; [f]College of Veterinary Medicine, China Agricultural University, Beijing 100193, China; [g]National Key Laboratory of Intelligent Tracking and Forecasting for Infectious Diseases, Chinese Center for Disease Control and Prevention, Beijing 102206, China; [h]Laboratory of Protein Engineering and Vaccines, Tianjin Institute of Industrial Biotechnology, Chinese Academy of Sciences, Tianjin 300308, China; and [i]Center of Infectious Disease, Beijing Ditan Hospital, Capital Medical University, Beijing 100015, China

Author contributions: Y.W. designed research; Z. Chang, D.G., L.L., J.S., G.Z., X.Z., F.W., C.L., B.O.O., and S.L. performed research; X.L., Z. Chen, and Y.W. contributed new reagents/analytic tools; Z. Chang, D.G., L.L., J.S., G.Z., Y.C., Y.H., H.X., J.Q., F.G., and Y.W. analyzed data; and Y.W. wrote the paper.

1. X. J. Yu *et al.*, Fever with thrombocytopenia associated with a novel bunyavirus in China. *N. Engl. J. Med.* **364**, 1523–1532 (2011).
2. Q. Liu, B. He, S. Y. Huang, F. Wei, X. Q. Zhu, Severe fever with thrombocytopenia syndrome, an emerging tick-borne zoonosis. *Lancet Infect Dis.* **14**, 763–772 (2014).
3. J. W. Seo, D. Kim, N. Yun, D. M. Kim, Clinical update of severe fever with thrombocytopenia syndrome. *Viruses* **13**, 1213 (2021).
4. W. Liu *et al.*, Case-fatality ratio and effectiveness of ribavirin therapy among hospitalized patients in china who had severe fever with thrombocytopenia syndrome. *Clin. Infect. Dis.* **57**, 1292–1299 (2013).
5. K. Liu *et al.*, Epidemiologic features and environmental risk factors of severe fever with thrombocytopenia syndrome, Xinyang, China. *PLoS Negl. Trop. Dis.* **8**, e2820 (2014).

6. H. Tani *et al.*, Efficacy of T-705 (Favipiravir) in the treatment of infections with lethal severe fever with thrombocytopenia syndrome virus. *mSphere* **1**, e00061-15 (2016).
7. Y. Wu *et al.*, Structures of phlebovirus glycoprotein Gn and identification of a neutralizing antibody epitope. *Proc. Natl. Acad. Sci. U.S.A.* **114**, E7564–E7573 (2017).
8. Y. Sun *et al.*, Nonmuscle myosin heavy chain IIA is a critical factor contributing to the efficiency of early infection of severe fever with thrombocytopenia syndrome virus. *J. Virol.* **88**, 237–248 (2014).
9. S. Halldorsson *et al.*, Structure of a phleboviral envelope glycoprotein reveals a consolidated model of membrane fusion. *Proc. Natl. Acad. Sci. U.S.A.* **113**, 7154–7159 (2016).
10. L. K. McMullan *et al.*, A new phlebovirus associated with severe febrile illness in Missouri. *N. Engl. J. Med.* **367**, 834–841 (2012).
11. J. H. Gear, Hemorrhagic fevers, with special reference to recent outbreaks in southern Africa. *Rev. Infect. Dis.* **1**, 571–591 (1979).
12. H. Hoogstraal, J. M. Meegan, G. M. Khalil, F. K. Adham, The Rift Valley fever epizootic in Egypt 1977–78. 2. Ecological and entomological studies. *Trans. R. Soc. Trop. Med. Hyg.* **73**, 624–629 (1979).
13. S. Halldorsson *et al.*, Shielding and activation of a viral membrane fusion protein. *Nat. Commun.* **9**, 349 (2018).
14. K. H. Kim *et al.*, An anti-Gn glycoprotein antibody from a convalescent patient potently inhibits the infection of severe fever with thrombocytopenia syndrome virus. *PLoS Pathog.* **15**, e1007375 (2019).
15. X. Wu *et al.*, A single-domain antibody inhibits SFTSV and mitigates virus-induced pathogenesis in vivo. *JCI Insight* **5**, e136855 (2020).
16. M. E. Davis-Gardner, B. Alfant, J. A. Weber, M. R. Gardner, M. Farzan, A bispecific antibody that simultaneously recognizes the V2- and V3-glycan epitopes of the HIV-1 envelope glycoprotein is broader and more potent than its parental antibodies. *mBio* **11**, e03080-19 (2020).
17. Y. Huang *et al.*, Engineered bispecific antibodies with exquisite HIV-1-neutralizing activity. *Cell* **165**, 1621–1631 (2016).
18. R. De Gasparo *et al.*, Bispecific IgG neutralizes SARS-CoV-2 variants and prevents escape in mice. *Nature* **593**, 424–428 (2021).
19. J. Li *et al.*, Membrane-proximal epitope facilitates efficient T cell synapse formation by anti-FcRH5/CD3 and is a requirement for myeloma cell killing. *Cancer Cell* **31**, 383–395 (2017).
20. M. Friedrich *et al.*, Regression of human prostate cancer xenografts in mice by AMG 212/BAY2010112, a novel PSMA/CD3-Bispecific BiTE antibody cross-reactive with non-human primate antigens. *Mol. Cancer Ther.* **11**, 2664–2673 (2012).
21. Z. Li *et al.*, An engineered bispecific human monoclonal antibody against SARS-CoV-2. *Nat. Immunol.* **23**, 423–430 (2022).
22. C. Li *et al.*, Broad neutralization of SARS-CoV-2 variants by an inhalable bispecific single-domain antibody. *Cell* **185**, 1389–1401.e18 (2022).
23. Z. Ku *et al.*, Engineering SARS-CoV-2 specific cocktail antibodies into a bispecific format improves neutralizing potency and breadth. *Nat. Commun.* **13**, 5552 (2022).
24. S. Du *et al.*, Cryo-EM structure of severe fever with thrombocytopenia syndrome virus. *Nat. Commun.* **14**, 6333 (2023).
25. Q. Wang *et al.*, Neutralization mechanism of human monoclonal antibodies against Rift Valley fever virus. *Nat. Microbiol.* **4**, 1231–1241 (2019).
26. Y. Wu *et al.*, A noncompeting pair of human neutralizing antibodies block COVID-19 virus binding to its receptor ACE2. *Science* **368**, 1274–1278 (2020).
27. Y. Q. Chen *et al.*, Influenza infection in humans induces broadly cross-reactive and protective neuraminidase-reactive antibodies. *Cell* **173**, 417–429.e10 (2018).
28. L. M. Weiner, J. C. Murray, C. W. Shuptrine, Antibody-based immunotherapy of cancer. *Cell* **148**, 1081–1084 (2012).
29. M. G. Rossmann, C. G. van Beek, Data processing. *Acta Crystallogr. D Biol. Crystallogr.* **55**, 1631–1640 (1999).
30. P. Emsley, K. Cowtan, Coot: Model-building tools for molecular graphics. *Acta Crystallogr. D Biol. Crystallogr.* **60**, 2126–2132 (2004).
31. P. D. Adams *et al.*, PHENIX: Building new software for automated crystallographic structure determination. *Acta Crystallogr. D Biol. Crystallogr.* **58**, 1948–1954 (2002).
32. S. Q. Zheng *et al.*, MotionCor2: Anisotropic correction of beam-induced motion for improved cryo-electron microscopy. *Nat. Methods* **14**, 331–332 (2017).
33. A. Punjani, J. L. Rubinstein, D. J. Fleet, M. A. Brubaker, cryoSPARC: Algorithms for rapid unsupervised cryo-EM structure determination. *Nat. Methods* **14**, 290–296 (2017).
34. T. Bepler *et al.*, Positive-unlabeled convolutional neural networks for particle picking in cryo-electron micrographs. *Nat. Methods* **16**, 1153–1160 (2019).
35. E. F. Pettersen *et al.*, UCSF Chimera–A visualization system for exploratory research and analysis. *J. Comput. Chem.* **25**, 1605–1612 (2004).
36. P. Emsley, B. Lohkamp, W. G. Scott, K. Cowtan, Features and development of Coot. *Acta Crystallogr. D Biol. Crystallogr.* **66**, 486–501 (2010).
37. P. D. Adams *et al.*, PHENIX: A comprehensive Python-based system for macromolecular structure solution. *Acta Crystallogr. D Biol. Crystallogr.* **66**, 213–221 (2010).
38. V. B. Chen *et al.*, MolProbity: All-atom structure validation for macromolecular crystallography. *Acta Crystallogr. D Biol. Crystallogr.* **66**, 12–21 (2010).
39. G. Grass, E. A. Neugebauer, Extracorporeal endotoxin adsorption in septic patients–does it work? *Crit. Care Med.* **32**, 1792–1793 (2004).
40. B. Q. Minh *et al.*, IQ-TREE 2: New models and efficient methods for phylogenetic inference in the genomic era. *Mol. Biol. Evol.* **37**, 1530–1534 (2020).
41. S. Kalyaanamoorthy, B. Q. Minh, T. K. F. Wong, A. von Haeseler, L. S. Jermiin, ModelFinder: Fast model selection for accurate phylogenetic estimates. *Nat. Methods* **14**, 587–589 (2017).
42. I. Letunic, P. Bork, Interactive tree of life (iTOL) v5: An online tool for phylogenetic tree display and annotation. *Nucleic Acids Res.* **49**, W293–W296 (2021).
43. Z. Chang, F. Gao, Y. Wu, Crystal structure of SFTSV Gn and antibody SF1. RCSB Protein Data Bank. https://www.rcsb.org/structure/unreleased/8WSN. Deposited 17 October 2023.
44. Z. Chang, F. Gao, Y. Wu, Crystal structure of SFTSV Gn and antibody SF5. RCSB Protein Data Bank. https://www.rcsb.org/structure/unreleased/8WSP. Deposited 17 October 2023.
45. Z. Chang, F. Gao, Y. Wu, Crystal structure of SFTSV Gc and antibody. RCSB Protein Data Bank. https://www.rcsb.org/structure/unreleased/8WSU. Deposited 17 October 2023.
46. Y. Wu, J. Q. Sun, bsAb3_Gn_Gc Complex protein. RCSB Protein Data Bank. https://www.rcsb.org/structure/unreleased/8WQW. Deposited 17 October 2023.